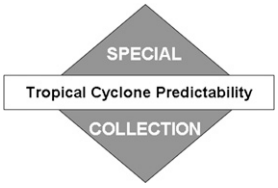

High-Definition Sounding System (HDSS) for Atmospheric Profiling

PETER BLACK,[a,h] LEE HARRISON,[b] MARK BEAUBIEN,[c] ROBERT BLUTH,[d] ROY WOODS,[d] ANDREW PENNY,[e] ROBERT W. SMITH,[f] AND JAMES D. DOYLE[g]

[a] *Surveillance and Reconnaissance Solutions Division, SAIC, Inc., Monterey, California*
[b] *Atmospheric Sciences Research Center, University at Albany, State University of New York, Albany, New York*
[c] *Yankee Environmental Systems, Inc., Turners Falls, Massachusetts*
[d] *Center for Interdisciplinary Remotely-Piloted Aircraft Studies, Naval Postgraduate School, Marina, California*
[e] *Meteorology and Physical Oceanography Department, Naval Postgraduate School, Monterey, California*
[f] *WB-57 Program Office, NASA Johnson Space Center, Ellington Field, Houston, Texas*
[g] *Marine Meteorology Division, Naval Research Laboratory, Monterey, California*

(Manuscript received 4 November 2014, in final form 30 December 2015)

ABSTRACT

The High-Definition Sounding System (HDSS) is an automated system deploying the expendable digital dropsonde (XDD) designed to measure wind and pressure–temperature–humidity (PTH) profiles, and skin sea surface temperature (SST) within and around tropical cyclones (TCs) and other high-impact weather events needing high sampling density. Three experiments were conducted to validate the XDD.

On two successive days off the California coast, 10 XDDs and 14 Vaisala RD-94s were deployed from the navy's Center for Interdisciplinary Remotely-Piloted Aircraft Studies (CIRPAS) Twin Otter aircraft over offshore buoys. The Twin Otter made spiral descents from 4 km to 60 m at the same descent rate as the sondes. Differences between successive XDD and RD-94 profiles due to true meteorological variability were on the same order as the profile differences between the spirals, XDDs, and RD-94s. XDD SST measured via infrared microradiometer, referred to as infrared skin SST (SSTir), and surface wind measurements were within 0.5°C and 1.5 m s^{-1}, respectively, of buoy and Twin Otter values.

A NASA DC-8 flight launched six XDDs from 12 km between ex-TC Cosme and the Baja California coast. Repeatability was shown with good agreement between features in successive profiles. XDD SSTir measurements from 18° to 28°C and surface winds agreed well with drifting buoy- and satellite-derived estimates.

Excellent agreement was found between PTH and wind profiles measured by XDDs deployed from a NASA WB-57 at 18-km altitude offshore from the Texas coast and NWS radiosonde profiles from Brownsville and Corpus Christi, Texas. Successful XDD profiles were obtained in the clear and within precipitation over an offshore squall line.

1. Introduction

Widely used tropical cyclone (TC) models include regional air–sea coupled dynamical models such as COAMPS-TC (Jin et al. 2014), HWRF (Tallapragada et al. 2014; Kim et al. 2014) and GFDL (Bender et al. 2007; Gall et al. 2011); global dynamical models such as GFS and ECMWF; and statistical–dynamical intensity-prediction models such as SHIPS, the Statistical Typhoon Intensity Prediction Scheme (STIPS), the Logistic Growth Equation Model (LGEM), and the rapid intensity index (RII; DeMaria and Kaplan 1999; DeMaria et al. 2005; Knaff et al. 2005; Jones et al. 2006; DeMaria 2009, 2010; Kaplan et al. 2010). These models stand to benefit from improved model and observational spatial and temporal resolution. Enhanced model resolution of smaller-scale physical processes, such as convective events, boundary layer air–sea transfer processes, and upper-troposphere outflow jets, will likely benefit to a greater degree from observational inputs at commensurate scales. Thus, observations and sampling strategies for initial condition

Denotes content that is immediately available upon publication as open access.

[h] Current affiliation: NOAA/OAR UAS Program Office Contractor, Cherokee Nation Technologies, LLC, Salinas, California.

Corresponding author e-mail: Peter G. Black, peter.black@noaa.gov

DOI: 10.1175/JTECH-D-14-00210.1

specification and forecast validation, similar to those employed in past TC field programs, such as, the Coupled Boundary Layer Air–Sea Transfer (CBLAST) experiment during the 2003/04 hurricane season, Tropical Cyclone Structure 2008 (TCS08), and Impact of Typhoons on the Ocean in the Pacific (ITOP) in 2010 (Black 2012; Black et al. 2007; D'Asaro et al. 2011, 2014), require continual improvement to match model demands. Improved data may also yield better process understanding and parameterizations for smaller scales.

New capabilities that the High-Definition Sounding System (HDSS) and expendable digital dropsonde (XDD) technology can provide to assist with TC science issues include the capability for deployment of many sondes in a rapid sequence, up to 40 sondes at the present time, over a small time window, opening up the possibility of "seeding" the inner core of a TC with a "burst" of dropsondes in the outflow layer and below, allowing the outflow winds to disperse the sondes throughout the TC inner core. In this way clusters of observations could be brought into the new generation of data assimilation schemes associated with new TC forecast models. In addition, such burst sampling can allow for resolution of strong gradients associated with outflow jet features and other high-gradient inner-core features that was never before possible. The XDD also provides the capability to observe the ocean infrared skin sea surface temperature (SSTir) coincident with the atmospheric profile observations. This is becoming an increasingly critical observational input as a new generation of coupled air–sea TC prediction models demand data inputs from the ocean as well as from the atmosphere.

The advent of GPS dropsonde atmospheric profiling (Hock and Franklin 1999; Franklin et al. 2003; Wang et al. 2015) has played a key role in contributing to this need and in demonstrating improved model track and intensity prediction performance (Burpee et al. 1996; Aberson and Franklin 1999; Wu et al. 2007; Weissmann et al. 2011; Aberson 2010, 2011; Chou et al. 2011; Wang et al. 2015). Dropsonde observations have also become the "reference standard" against which airborne remote wind sensors such as the Stepped Frequency Microwave Radiometer (SFMR) have been validated, resulting in improved hurricane intensity estimation and the use of SFMR as the "gold standard" for hurricane surface wind measurement (Uhlhorn and Black 2003; Uhlhorn et al. 2007; Klotz and Uhlhorn 2014). However, despite recent advanced observational technology and model advancement, there has been only small improvement in official predictions of TC intensity, either in the Atlantic or Pacific basins (DeMaria et al. 2014).

The HDSS has been validated during a series of collaborative test flights with 1) Naval Postgraduate School, Center for Interdisciplinary Remotely-Piloted Aircraft Studies (CIRPAS), using their Twin Otter aircraft; 2) NASA Wallops Flight Facility (WFF), using their P-3 aircraft; 3) NASA Armstrong Flight Research Center (AFRC), using their DC-8 Airborne Science Laboratory; and 4) NASA Johnson Space Center–Ellington Field (JSC-EFD), using their WB-57 aircraft. Results presented are based on two Twin Otter flights with XDD deployments from 4-km altitude, one DC-8 flight with XDDs deployed from 12-km altitude, and three WB-57 flights with deployments from 18-km altitude. These tests were conducted, respectively, from 1) the CIRPAS facility in Marina, California, over National Data Buoy Center (NDBC) buoys offshore from the northern California coast; 2) AFRC in Edwards, California, over the eastern Pacific east of TC Cosme and southwest of Cabo San Lucas, Mexico; and 3) JSC–Ellington Field, Texas, over the western Gulf of Mexico offshore from the Texas coast adjacent to NWS radiosonde stations at Brownsville (BRO) and Corpus Christi (CRP) and NDBC buoys.

2. XDD/HDSS description

The HDSS is the integrated system of antennas, receivers, and telemetry that receives data from XDDs deployed by the Automated Dropsonde Dispenser (ADD) and then telemeters that data to the ground. The XDD measures GPS location and altitude, and vertical profiles of pressure–temperature–humidity (PTH) at 2-Hz rate, horizontal wind velocity, and sonde fall speed at 4 Hz, as well as SSTir at 1 Hz. Instruments used to obtain PTH are a pressure transducer, fast-response thermistor with digital oversampling, and a relatively slow-response hygrometer. SSTir is measured with an infrared microradiometer at 8–12-μm wavelength. HDSS derives GPS location and winds from state-of-the-art u-blox chip technology for the Twin Otter flights in 2011 and for the DC-8 and WB-57 flights in 2013, incorporating the latest changes and improvements inherent in the proprietary GPS tracking technology between 2011 and 2013. System and sonde instrument specifications are summarized in Tables 1 and 2. From comparison of these tables with those in Hock and Franklin (1999) and Wang et al. (2015), we conclude that the XDD wind accuracy is similar to that of the RD-94. The physical layout of the XDD prototype and new sheath used after 2013 are shown in Figs. 1a,b.

These are manufacturer accuracy specifications. Not enough sondes had been built during the testing period described in this paper to develop a statistically significant database of actual error specifications derived from laboratory testing. Because laboratory testing is not available at this time, it is impossible to differentiate between pure instrument error and atmospheric variability.

TABLE 1. XDD System Specifications

Parameter	Power	Weight	Dimensions	Wind Type/Rate	Digital Encoding	RF[a] Power	Antenna Type	Forward Error Correction Update Rate	Number of Simultaneous Soundings
Value	CR2 lithium battery	58 g	6.6 cm in diameter by 17.8 cm long	12-sat GPS/ 4–1 Hz[b]	FM FSK[c]	10 mW	Quadrafilar	1 Hz	42 per ADD, 2 ADD[d], 84 per HDSS

[a] RF: Radio frequency
[b] Early sonde data rate for Twin Otter and DC-8 flights
[c] FM FSK: Frequency modulation frequency-shift keying
[d] ADD: Automated dropsonde dispenser

Here we seek only to determine the overall variability of the coupled system as a first step toward full analysis of instrument sensitivity and measurement uncertainty. As indicated above, the hundreds of instruments constructed and deployed since the present initial trial study was done have provided meaningful new data on instrument uncertainty that will be analyzed in the future.

As stated in Hock and Franklin (1999) and in Wang et al. (2015), RD-94 has the following specifications: Pressure accuracy of 0.5 mb, precision of 0.1 mb; temperature accuracy of 0.2°C and precision of 0.1°C; humidity accuracy of 2%, precision of 0.1%; and GPS wind speed (WS) accuracy of 0.5 m s^{-1}, precision of 0.2 m s^{-1}. As many as eight RD-94 sondes can be operated simultaneously.

The initial development of the XDD was known as the expendable digital radiosonde (XDR) and was tested on the NASA DC-8 during the Arctic Mechanisms of Interaction between the Surface and Atmosphere (AMISA) in 2008. A total of 36 XDRs were deployed over 6 days. Comparison with simultaneous radiosonde ascents from the Swedish Icebreaker *Oden* showed good results (Gasiewski et al. 2009; Persson 2010).

Modern XDD sondes are activated and programmed before launch via a noncontact optical interface to select communication parameters prior to release. The XDD contains no parachute and its center of gravity can be adjusted to select either a ballistic fast-fall or spiral-dive slow-fall mode of descent. Grooves etched into the rigid polystyrene plastic printed circuit board (PCB) housing (Fig. 1a) provide air pathways between the foam and the cardboard sheath to maintain spiral descent. Sea level descent rates are approximately 18 m s^{-1} for the fast-fall sondes and 10 m s^{-1} for the slow-fall sondes, with the former having greater stability. All sondes deployed from the CIRPAS Twin Otter were slow-fall sondes, with the goal of matching RD-94 descent rates. Based on XDDs deployed in May 2015 during the recent polar winds experiment (D. Emmitt 2015, personal communication), slow-fall spiral descent rotation rates appeared to be on order of 0.9–1.2 s^{-1} based on observed sonde descent rate modulation. The displacement radius of the sonde during rotation was on order of 1 m.

Later XDD versions deployed by the WB-57 measured vertical profiles of pressure–temperature–humidity (PTU) at 2 Hz, GPS-derived velocities at 4 Hz, and SSTir at a 1 Hz. Longitude and latitude and "housekeeping" data are reported at lower rates (~0.1 Hz). Earlier XDD versions deployed from the Twin Otter and from the DC-8 reported all variables at 1 Hz.

The configuration of HDSS evolved for each of the four aircraft installations as various components were developed and improved. The prototype HDSS installation on the Twin Otter had a single dispenser with a 48-sonde magazine and one receiver. Subsequent improvements to HDSS were implemented for the DC-8 flights that involved hardening of the dispenser for pressurized aircraft.

The DC-8 deployments from 12-km altitude were done with manual release to demonstrate the survival of

TABLE 2. XDD Sensor Specifications

Parameter	Sensor type/data rate	Range	Accuracy	Resolution
Temperature	Thermistor/2 Hz/1 Hz[a]	−90° to 50°C	±0.14°C	0.016°C
Pressure	MEMS[b]/2–1 Hz[a]	150–1150 hPa	±1.5 hPa at 25°C	±2.5 hPa
Humidity	MEMS[b]/2–1 Hz[a]	10%–100% for temperature > −37°C	1.8% at 25°C	0.1%
Sea surface temperature	Infrared micro-radiometer, 9–11 μm/1 Hz	0°–50°C	±0.2° at 25°C	0.016°C

[a] Early sonde data rate for Twin Otter and DC-8 flights
[b] MEMS: Microelectromechanical System

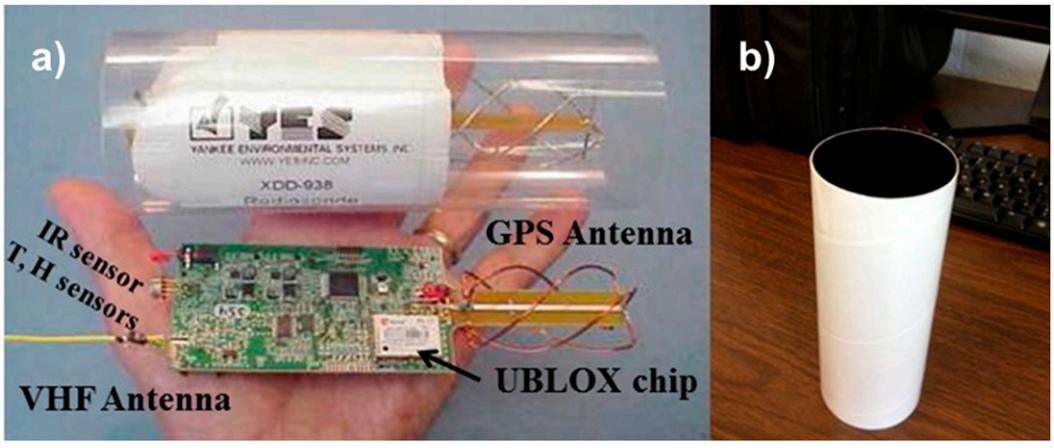

FIG. 1. (a) Earlier XDD version used in the CIRPAS Twin Otter experiment. Its outer sleeve was clear plastic, showing the foam inner body within. The PCB is shown with uncoiled telemetry, and GPS antennas and sensor locations. (b) The new XDD sheath into which the foam PCB casing is inserted, as well as the improved PCB with a revised electronic design and antenna assembly. The new sheath is a biodegradable cardboard cylinder coated black inside and white outside to minimize radiation effects. Weight is 58 g, and size is 17.8 cm long by 6.6 cm in diameter.

the XDDs from flights at high indicated airspeed (IAS), that is, $>250\,\mathrm{m\,s^{-1}}$. In addition, operation of forward error correction (FEC) on two receivers was implemented to improve data reception at ranges > 200 km. Beyond sensor uncertainties, overall data quality is affected by data gaps in the telemetered data. To minimize gaps, the XDD uses FEC to recover data packets having bit errors. In addition, merged data from four redundant receivers minimizes overall data dropouts that appear at different times on the four different receivers, providing a more continuous stream of observations for use in optimal time series filtering. This technology becomes important at high altitudes (>18 km), where line-of-sight transmission pathlengths from aircraft to sonde can be >200 km from WB-57 or DC-8 flights.

FEC algorithms such as Viterbi (Gupta et al. 2010) use additional bandwidth to send along specially encoded extra data bits with the data payload. At the telemetry receiver, a mathematical decode algorithm reconstructs the dataset from a corrupted packet using the extra FEC data. The first XDD system tested at CIRPAS had a single receiver with five channels and no FEC but the pathlength was only 3.7 km. The DC-8 test introduced FEC and time-division multiplexing (TDM). The WB-57 tests demonstrated quad-redundant receivers and antennas, enabling aircraft maneuvers without data loss during XDD descents. TDM effectively increases the number of XDDs that can be in flight simultaneously, where each of five telemetry receiver channels accommodates eight time slices. With eight time slices and five channels, reception from up to 40 XDDs can be supported simultaneously from each of four receivers. Finally, a sixth backup spare channel is available that can be used to monitor the local radio spectrum for sources of interference.

Further improvements to HDSS were implemented for flights flown on the WB-57 in 2013, one of which consisted of implementing two separate dispensers. Paired dispensers allow launch rates faster than once every 5 s if needed and provide redundancy to enhance reliability in case one dispenser jams or fails. The paired dispensers for the improved HDSS have a magazine forebody that holds 12 sondes on each side, with an optional magazine extender to accommodate 48 on each side (96 in total). There was no need for the extenders in 2013 given the limited number of sondes deployed. Each of the two dispensers has a receiver and a control computer, which were fed from an antenna and preamplifier mounted on the underbelly of the WB-57 pallet. The two receivers connected to antennas mounted near the wingtips of the aircraft allow signals to be received during aircraft turns when the large wing would result in shadowing of the two belly antennas and receivers.

The HDSS also carries two cameras to record dropsonde ejection: one aft of the drop tubes facing forward and one forward of the drop tubes facing aft. These cameras also were used to document cloud structures ahead of and behind the aircraft (Fig. 16). The mission monitor display for the WB-57 was used to maintain situational awareness of XDD status in the dispensers, as well as postlaunch status and parameter display.

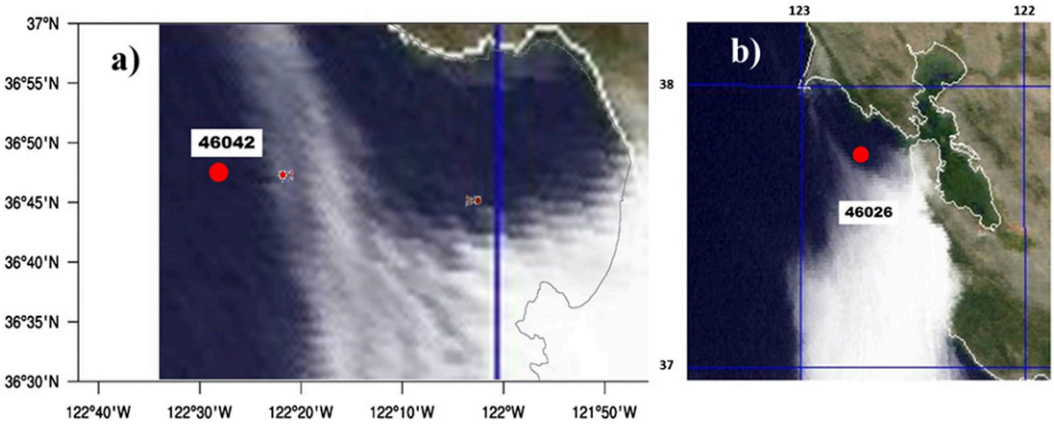

FIG. 2. (a) Visible satellite image over Monterey Bay showing stratus cloud cover and NDBC buoy 46042 location (small red dot to the east of the buoy) at the time of the Twin Otter dropsonde intercomparison deployments on 24 Jun. (b) A visible satellite image over San Francisco Bay showing stratus cloud cover and NDBC buoy 46026 location (red dot) at the time of the Twin Otter dropsonde intercomparison flight on 25 Jun. Blue lines are latitude and longitude lines on the original image. (Courtesy of NRL satellite image archive: http://www.nrlmry.navy.mil/sat-bin/epac_westcoast.cgi.)

3. Twin Otter HDSS/XDD evaluation experiment

The first experiment used the Naval Postgraduate School (NPS) CIRPAS Twin Otter operating from Marina, California. XDD data are compared with the instrumented research aircraft, Vaisala RD-94 dropsondes, and NDBC surface buoys. The locale provided nearby NDBC moored buoys and an atmosphere with large changes in temperature and humidity across the top of the offshore marine layer in order to test instrument response in strong gradients. Twin Otter flights were conducted on 24 and 25 June 2011, when only minimal low-level cloud cover was present at the top of the marine layer near the buoy locations; GOES-West visible satellite cloud images for overflight times on these 2 days adjacent to Monterey Bay and San Francisco Bay are shown in Figs. 2a,b. Both show nearby layers of low stratocumulus clouds.

The Twin Otter standard meteorological instrumentation package (H. Jonsson 2012, personal communication) was utilized with aircraft spiral descents/ascent at the same rate as the dropsonde fall rates and served as the reference. The Twin Otter provided two deployment tubes: one designed to launch standard dropsondes and another to launch airborne expendable bathythermographs (AXBTs) or sonobuoys. The latter was sleeved for the XDD dropsondes so that simultaneous deployment of RD-94 and XDD dropsondes was possible. A standard NCAR Airborne Vertical Atmospheric Profiling System (AVAPS), part of the Twin Otter instrumentation suite, was used for the RD-94s.

All analysis of RD-94 data was done using the raw "D" files generated by AVAPS. The goal of this analysis was to compare profiles without any postprocessing or filtering. Telemetry errors for both systems were artificially low in these flights because the aircraft was never more than a few kilometers away from the sondes during descent.

Two NDBC moored buoys were chosen as a second reference standard for comparison of surface meteorological variables. The tests consisted of dual launches of the RD-94 and XDD sondes within 10 s of each other from 4-km altitude over NDBC buoy 46042 off Monterey Bay on 24 June and from 4-km altitude over NDBC buoy 46026 off San Francisco Bay on 25 June. The dual launches were followed immediately by the spiral descent of the aircraft at a rate close to that of the sondes. XDD slow-mode fall rates without a parachute are similar to RD-94 fall rates with a parachute.

Aircraft flight patterns were designed so that pairs of RD-94 and XDD sondes were deployed from 4-km altitude followed immediately by aircraft spiral descents to 60 m at approximately the fall rate of the sondes, which were nearly equal to each other, at 10–12 m s^{-1}. This was accomplished on both days followed by a slower ascent back to 4-km altitude with 2-min straight and level legs upwind and downwind at six levels during the ascent. This latter maneuver determined aircraft true airspeed and wind errors. Corrections were applied resulting in aircraft winds independent of heading during spiral descents.

a. Comparison between XDD and RD-94 dropsonde profiles and NDBC buoy data

Figures 3a,b show three-point weighted smoothed air temperature profiles for 25 June over buoy 46026 for three Yankee Environmental Systems XDDs and a

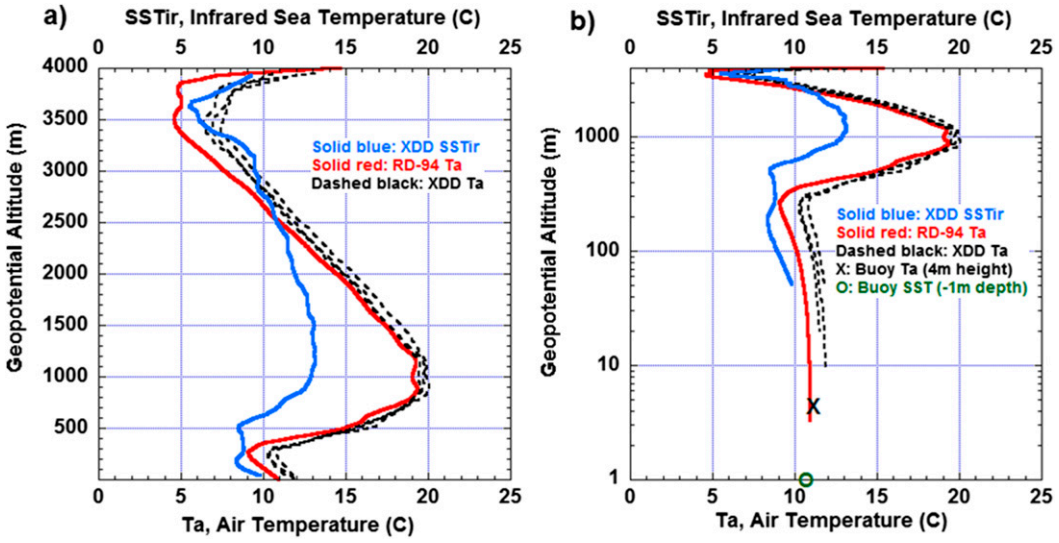

FIG. 3. Comparison between XDD and RD-94 dropsonde profiles of air temperature Ta deployed from CIRPAS Twin Otter aircraft on 25 Jun 2011 offshore from San Francisco Bay over NDBC buoy 46026: (a) linear geopotential height coordinates and (b) log height coordinates, emphasizing boundary layer detail. XDD "effective" SSTir profile, as well as buoy-observed Ta at 4-m elevation and bulk SST at −1-m depth. All profiles were smoothed with a three-point, triangular-weighted running "Bartlett" filter (five-point, 1.25-s window).

typical Vaisala RD-94 sonde. The temperature plots in Fig. 3a indicate an XDD sonde-to-sonde variance of ±0.7°C and a profile mean XDD warm bias relative to RD-94 mean temperature profiles averaging +1.2°C, in close agreement with bias estimates relative to the surface buoy observations as well as Twin Otter aircraft profile observations discussed in section 3b. Also shown is the sonde miniradiometer SSTir profile typical of one of the XDDs. The observed values in the profile indicate the sum total of true SSTir plus intervening atmospheric water vapor and cloud attenuation. Linear extrapolation of the lowest 150-m values to the surface (not shown) indicate the sonde best estimate of SSTir, agreeing to within 0.5°C of NDBC buoy 46026 bulk SST measurements at the same time at a depth of 1 m. A nine-point smoother was used for SSTir, as well as for pressures and winds.

Figures 4a,b show the three-point weighted smoothed air temperature profiles as in Fig. 3a and corresponding humidity profiles for 25 June over buoy 46026 as a function of geopotential altitude (GA). XDD sondes indicate a small warm bias for XDD relative to RD-94 of 0.5°–1.0°C throughout the profile with larger biases of 1°–3°C in the upper levels between 3 and 4 km (seen best in the Fig. 3a linear height plot). This appears to be due to a larger lag of the XDD air temperature sensor in adjusting to the change from the aircraft temperature to the outside air temperature.

Both sondes required lags of about 15 s, or about 200 m vertically, to acclimate to the outside environmental temperature just after release from the aircraft. XDD biases (>1°C) relative to RD-94 were also observed within the marine layer, best seen in Fig. 3b. Extrapolation of data in the lowest 150 m to the 4-m elevation buoy air–temperature observation yields an RD-94 air temperature about 0.25°C cooler than the buoy temperature of 11°C, with the XDD about 0.75°C warmer. The 20°C air temperature maximum at the top of the inversion and the 10°C minimum at the base of the inversion are well resolved by both sondes.

The humidity sensor used in the XDDs at the CIRPAS intercomparison is slower than the sensor used in the RD-94s. Nonetheless, a comparison of humidity profiles in Figs. 4a,b between RD-94 and XDD sondes shows consistent features in the humidity measurements: 1) the upper moist layer at the base of a temperature inversion (3–3.5 km; Fig. 4a); 2) the dry adiabatic layer from the top of the marine layer inversion (1.25 km) to the base of the upper moist layer (2.7 km); 3) the strong moisture gradient from the top of the marine layer inversion to the top of the adiabatic marine layer (250 m); and 4) the cool, moist adiabatic marine layer at constant humidity (250 m to the surface; Fig. 4b). The primary difference between the RD-94 and XDD humidity profiles is that the XDD profiles are about 5% wetter than the RD-94 in the upper levels (Fig. 4a) and about 10% drier within the marine layer below 500 m (Fig. 4b). This behavior together with the slow response of the sensor to abrupt changes in the humidity structure at the top of the marine layer at 300 m suggests a much slower response of the XDD

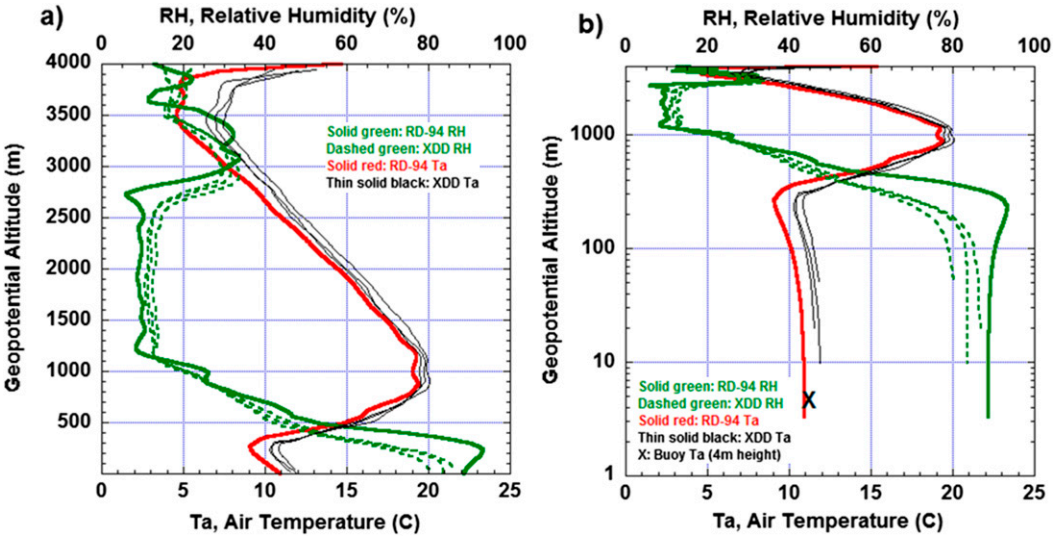

FIG. 4. Comparison between XDD and RD-94 dropsonde profiles from CIRPAS Twin Otter aircraft of Ta and RH on 25 Jun 2011 offshore from San Francisco Bay over NDBC buoy 46026: (a) linear geopotential height and (b) log geopotential height, designed to emphasize boundary layer detail. All profiles were smoothed with a three-point, triangular-weighted running Bartlett filter (five-point, 1.25-s window).

humidity sensor than seen from the RD-94 humidity sensor and from the aircraft humidity sensor during the spiral descent discussed in the next subsection.

Both XDDs and RD-94 observe interesting oscillations of the wind speed with height, shown in Figs. 5a,b, and wind direction (WD) with height, shown in Figs. 6a,b, which were associated with the features described above in the temperature profile. The RD-94 and XDD wind speeds and directions are similar to each other with a mean speed variance of 1 m s^{-1} and a mean direction variance of 5°. The most prominent of these features are 1) the upper-level wind maximum

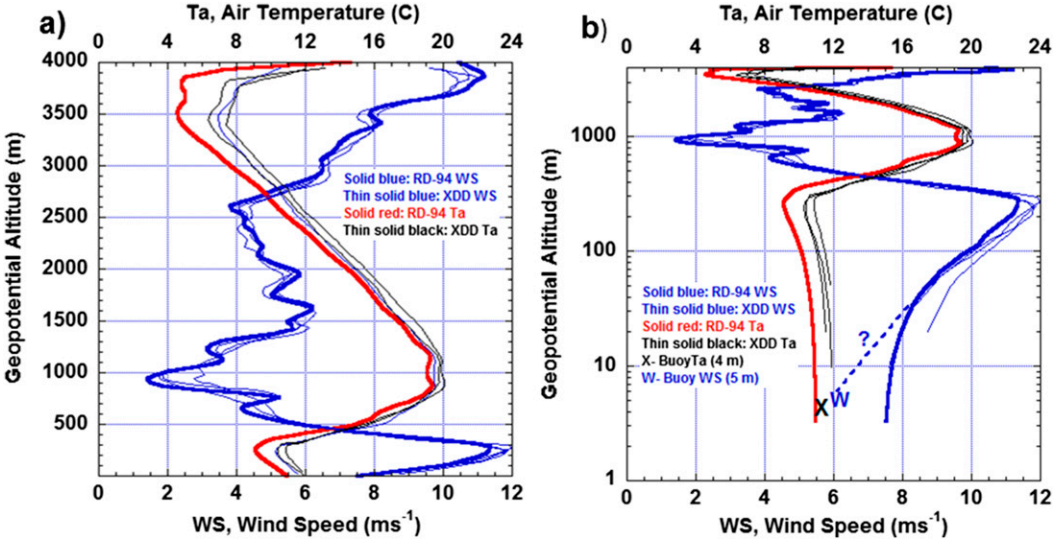

FIG. 5. Comparison between XDD and RD-94 dropsonde profiles from CIRPAS Twin Otter aircraft of Ta and WS on 25 Jun 2011 offshore from San Francisco Bay over NDBC buoy 46026: (a) linear geopotential height and (b) log geopotential height, designed to emphasize boundary layer detail. Dashed blue line indicates log-law extrapolation of upper boundary layer winds to the 5-m level. All profiles were smoothed with a three-point, triangular-weighted running Bartlett filter (five-point, 1.25-s window). Buoy temperature and WS observations are indicated by black "X" and blue "W," respectively.

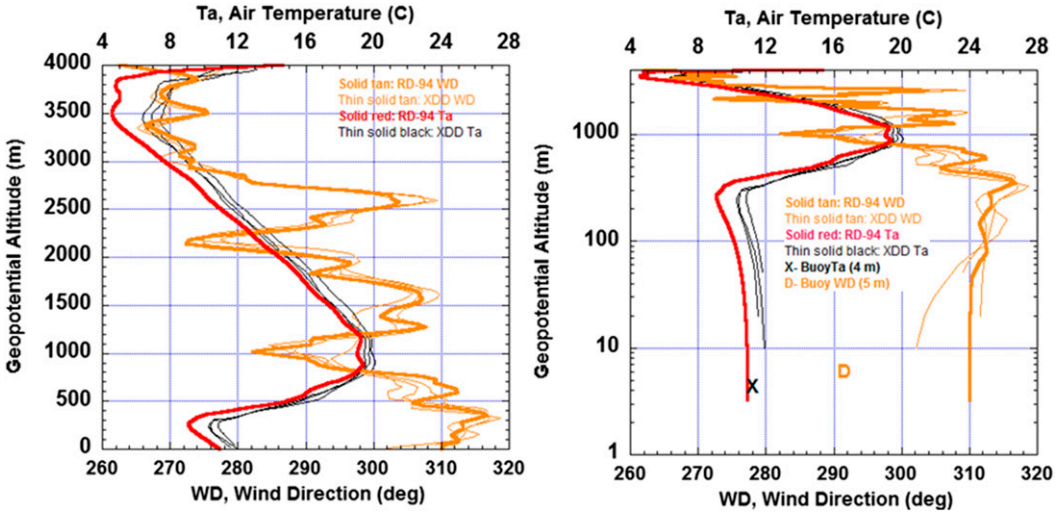

FIG. 6. Comparison from CIRPAS Twin Otter aircraft between XDD and RD-94 dropsonde observations of Ta and WD for 25 Jun 2011 with (a) linear geopotential height coordinates and (b) log coordinates, emphasizing boundary layer detail. RD-94 data are denoted with bold red and tan, XDD data are denoted with thin black and tan. Symbol X is air temperature, and symbol D is WD from NDBC buoy 46026 at the time of the overflight and sonde drops, approximately 2050 UTC.

(3.8 km) at the top of the upper inversion (3.5–3.7 km); 2) the weak wind shear throughout the upper half of the adiabatic layer (3.5–2.6 km) down to the top of the very dry layer at 2.5 km; 3) the nearly constant wind speed throughout the dry layer (2.7–1.25 m), despite considerable directional fluctuations; followed by 4) the most prominent speed and directional shear layer from 0.9- to 0.3-km altitude with a wind maximum at the top of the marine inversion at 1 km. It is interesting to note that in the satellite images (Figs. 2a,b) for both 24 and 25 June, wavelike features with a constant wavelength of 2.3 km can be observed in the stratus clouds, typical of Kelvin–Helmholtz instability associated with strong shear in the cloud layer just below the marine inversion. And finally, the sondes observe a frictional shear layer throughout the adiabatic marine layer following the log law to 35 m, below which a constant wind with height layer is observed primarily from the RD-94, with XDD data terminating prematurely at 30–50 m, a result of 1-Hz data rates compared to 4 Hz from the RD-94. Corresponding to the wind speed features in Figs. 5a,b, there is little directional shear of the wind shown in Figs. 6a,b within the upper wind maximum and the upper inversion layer. However, strong directional shear accompanies the wind speed shear within the upper adiabatic layer extending to the top of the dry layer at 2.5 km. Then, in contrast to the constant wind with height in the dry layer in Figs. 5a,b, the wind direction shown in Figs. 6a,b oscillates through two cycles of 30° direction changes, reaching a minimum just at the top of the marine layer inversion. Strong directional shear accompanies the strong speed shear throughout the inversion extending to the wind maximum at the top of the marine adiabatic layer.

Within the marine layer, the wind rotates clockwise with decreasing height below the wind maximum due to near-surface frictional effects. Therefore, not only are the observations repeatable and consistent between sonde types, but the observations are also consistent with typical meteorological features observed above and below the marine layer offshore from the central California coast.

b. Comparison of XDD and Twin Otter observations

Figure 7 shows comparison profiles between XDD sonde and Twin Otter air temperature and humidity profiles (Fig. 7a), wind speed and wind direction profiles (Fig. 7b), and SSTir (Fig. 7c). As shown in the comparison with the RD-94 (Figs. 4a,b), there is a lag in response of both XDD temperature and humidity compared with the Twin Otter, as well as a slight warm and dry bias on the order of 1°C and 5%, respectively. The cool, moist marine layer overlaid by a warm, very dry midlevel air mass is well resolved by both XDD and Twin Otter. Agreement is also evident in Fig. 7b between the respective wind speed and wind direction profiles, with vertical spatial scales in the midlevels on the order of 500 m or less being well resolved. Both XDD and Twin Otter observations resolve the low-level wind maximum at the top of the marine

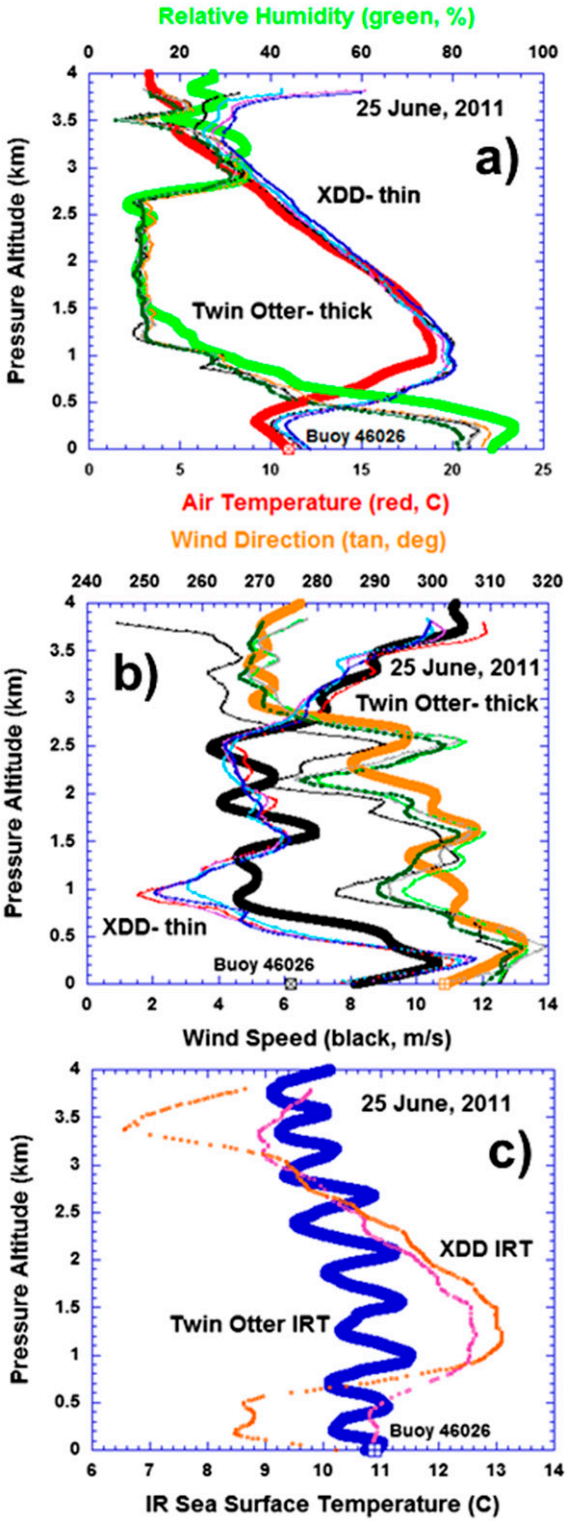

FIG. 7. Comparison of XDD sonde profiles (thin lines) with Twin Otter aircraft profiles (thick lines) during spiral descent on 25 Jun over buoy 46026 of (a) temperature and relative humidity, (b) WS and WD, and (c) sea surface temperature. Squares with imbedded x indicates buoy observations.

layer. Observations from XDD sondes each resolve the same features as shown in the Twin Otter profiles, demonstrating good repeatability of the measurements.

The SSTir profile measurements provided by the XDDs, shown in Fig. 7c compared with the Twin Otter SSTir profile measurements, are obtained from an infrared microradiometer operating in the 8–12-μm ''water vapor window'' infrared (IR) band. This window is not entirely transparent to atmospheric water vapor and oxygen, the two main atmospheric emission sources in this band. The Twin Otter was equipped with an Infrared Radiation Radiometer (IRT) covering a narrower IR band from 9 to 11 μm, which is somewhat less sensitive to water vapor. The oscillation of the Twin Otter SSTir during the descent, superimposed onto a linear increase, suggests the possibility that the spiral descent occurred near a cloud boundary.

The XDD SSTir shows a profile shape similar to air temperature and humidity, suggesting a stronger dependence on these quantities than the Twin Otter IRT. The SSTir is estimated from linear extrapolation of the lowest 150-m layer of sonde-reported values, where column water vapor contributions are small. Below 100 m both XDD and Twin Otter SSTir values approach similar values of approximately 12.5°C, in good agreement with buoy 46042 ''bulk'' SST observations at 1-m depth of 13°C. Further, surface conditions observed by buoy 46042 at the sonde deployment date and time of 2050 UTC 26 June indicated the winds were 6.2 m s^{-1} and significant wave heights were 2 m and decreasing with time. There was also a 6-s period swell propagating across the region from 310°. These conditions occurring during late afternoon were likely to provide sufficient mixing in the near-surface layer, so that skin and bulk SST measurements would be nearly equal.

4. DC-8 XDD observations

The DC-8 XDD deployments were a piggyback mission on a NASA flight to monitor a satellite launch from Vandenberg Air Force Base, California. The sonde deployments were made on the return leg of a north–south flight leg from 12° to 21°N, approximately along 119°W, directly along a dry air intrusion to the east of the former Tropical Storm Cosme, and extending across a strong SSTir gradient of 22°–27°C, as shown in Figs. 8a,b. Three fast-fall sondes (light blue, magenta, and light gray symbols) with sea level fall speeds of 17 m s^{-1} were deployed from 0300 to 0330 UTC 28 June 2013 followed by three slow-fall sondes from 0330 to 0400 UTC 28 June (blue, red, and dark gray symbols) with sea level fall speeds of 10 m s^{-1}.

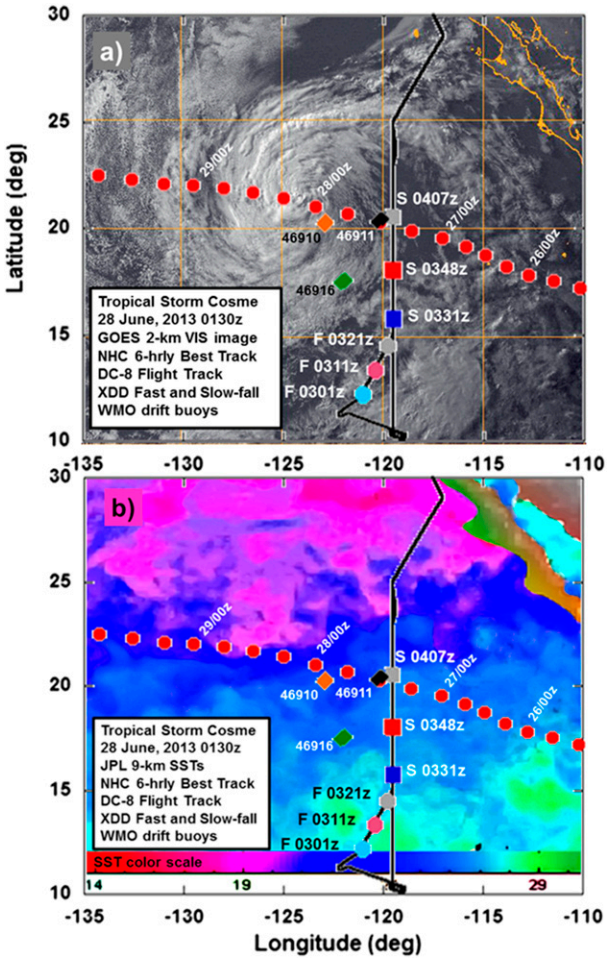

FIG. 8. (a) GOES visible satellite image of former Tropical Storm Cosme for 0130 UTC 28 Jun 2013. Cosme's NHC-derived best-track 6-hourly positions from 1200 UTC 25 Jun to 0000 UTC 30 Jun are shown by the solid red circles. The NASA DC-8 flight track is in black with outbound and return legs overlapping north of 15°N. During the return leg, three fast-fall XDDs were deployed along the diagonal flight leg from 13° to 15°N, indicated by the sky blue, magenta, and gray circles from 0301 to 0321 UTC. These were followed by the deployment of three slow-fall XDDs, indicated by the solid navy blue, red, and gray squares from 0331 to 0407 UTC. In addition, the locations of three WMO SST drifting buoys are indicated by black (46911), tan (46910) and green (46916) diamonds. (b) Enhanced high-resolution satellite IR SST map for 28 Jun with Cosme's track, DC-8 track, XDD fast- and slow-mode sonde locations, and drift buoy locations superimposed as in (a).

Drops relative to Cosme's center ranged from 1000 km south-southeast for the first sonde to 450 km east-southeast for the last sonde, which was at the DC-8 point of closest approach to Cosme's center. Figures 8a,b also show the location of three Argo SST drifting buoys, one of which was located only 20 km from the last drop. Ground truth estimates of SSTir from this satellite product as well as from the drift buoy observations of bulk SST showed agreement with the sonde SSTir to within 0.5°C over a range of SSTs from 22° to 27°C. The XDD SSTir profiles for fast- and slow-fall sondes in Fig. 8c behaved about the same despite the different fall rates and form of descent (fast ballistic vs slow spiral dive). As with the Twin Otter–deployed XDD SSTir observations, the DC-8 XDD SSTir values also showed a pattern that reflected changes in air temperature and humidity during descent.

Surface winds from AMSU and ASCAT satellite sensors near 0000 UTC 25 June, about 3 h prior to the sonde deployments (not shown), indicate that surface winds along the DC-8 flight track were between 7 and 10 m s^{-1}. This was, once again, a strong enough wind to produce some limited whitecapping from breaking waves, mixing the ocean upper layer and minimizing differences between skin and bulk SST.

The fast-fall sondes traveled only 3.5–4.0 km to the north and northeast, consistent with upper southeast winds shifting to lower southwest winds. However, the slow-fall sondes traveled 9–12 km before splash; they traveled almost as far horizontally as they did vertically (13 km).

The DC-8 was the first flight test of the new telemetry protocols using FEC. Telemetry of the fast-fall data lost less than 1% of observations. The slow-fall XDDs lost upward of 20% of observations as a consequence of the varying transmit antenna orientation due to sonde spiral descent and extreme line-of-sight ranges greater than 150 km. A comparison of raw (unsmoothed) fall speed data between fast- and slow-fall XDDs is shown in Fig. 9a. One of the differences between slow- and fast-fall sondes is the greater variance in the slow-fall sonde fall speeds than with the fast-fall sondes. This is most likely due to the large-inclination spiral descent of these slow-fall sondes relative to the straight ballistic descent of the fast-fall sondes. This inclination of the slow-fall sonde GPS antenna with respect to satellite line of sight appears to result in more data gaps and greater descent rate variability. In contrast, the fast-fall sondes maintain their orientation with respect to GPS satellite location and maintain a relatively constant detection efficiency. This same situation applies to derived GPS winds as will be shown below.

Inspection of the air temperature as well as SSTir profiles in Figs. 9b,c show that sharp changes measured by these sensors in the vicinity of an inversion layer at 1.5 km are well resolved and do not depend on the sonde fall rate to be resolved. This suggests an adequate instrument response to resolve important small-scale atmospheric features. However, the slow-fall sondes, while exhibiting roughly the same variance as the fast-fall sondes, do

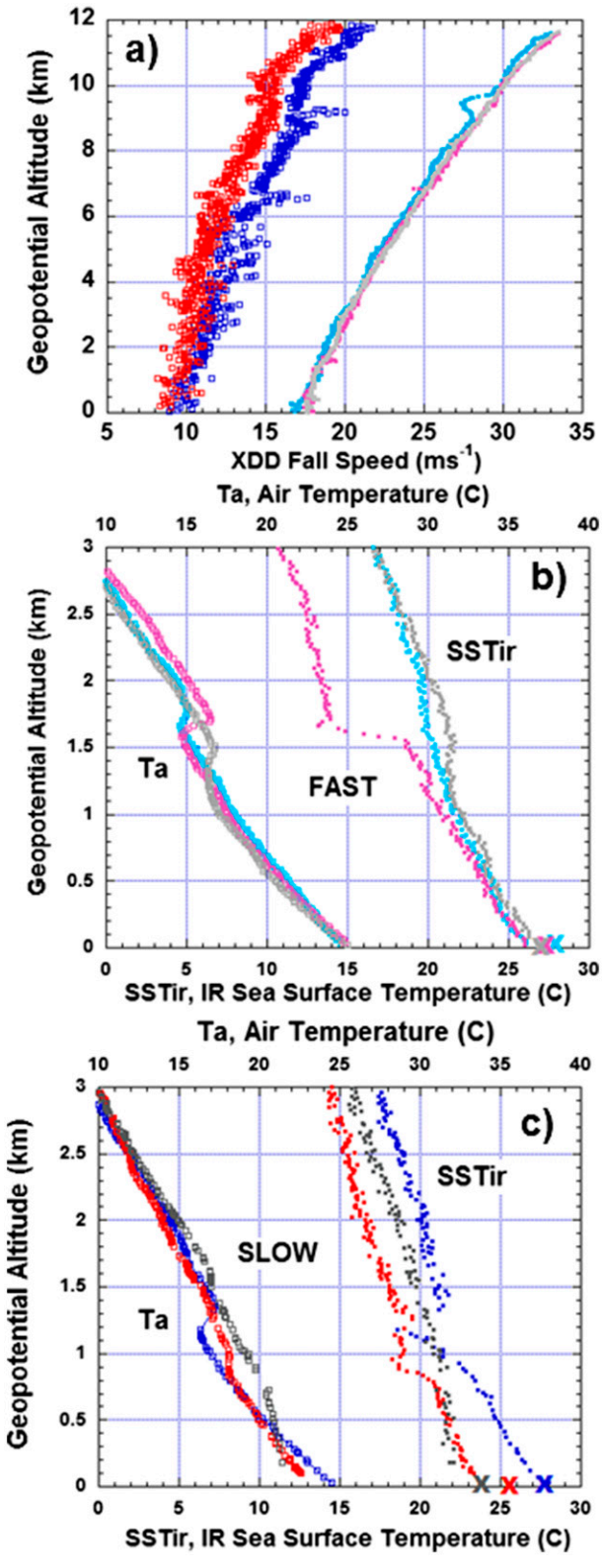

FIG. 9. (a) Slow- and fast-mode XDD fall speeds, and (b) lowest 3 km of fast-mode IR SST and Ta profiles, color-coded as with XDD locations in Figs. 8a,b. (c) Slow-mode IR SST and Ta profiles.

experience greater data dropouts in the low levels due to a longer distance from the aircraft (>150 km).

The humidity profiles for fast- and slow-fall sondes (Fig. 10a,b) show very little difference in variance between fast- and slow-fall sondes to the extent that there appears to be some internal instrument filtering in the hygrometer. However, the slow instrument response is reflected in the smooth character of the profiles. The humidity maximum from 6 to 7 km, suggestive of a cloud layer, together with the dry layer just below at 4–5 km is well resolved. The detailed structure within the boundary layer below 1 km appears to exhibit the same characteristic as the Twin Otter humidity profiles within the California marine boundary layer, that is, a slow measured response to a presumed rapid change in marine layer humidity compared to the relatively drier layer aloft. A relatively dry near-surface layer varies from 78% at the two southernmost fast-fall XDD locations to 93% at the four northernmost XDD locations and is consistent with the enhanced low-level moisture closer to Cosme's outer circulation.

The derived parameters of potential temperature and equivalent potential temperature, θ and θe, respectively, for fast- and slow-fall DC-8 XDDs are shown in Figs. 11a,b. They show similar structures from sonde to sonde with little difference between fast-fall and slow-fall sondes. The similar small-scale features seen in successive θe profiles suggest that realistic features are being resolved and that the measurements are repeatable.

Figures 12a,b show the raw XDD wind speed and direction profiles for the fast- and slow-fall sondes. Fast-fall XDDs observe double wind maxima just above the top of the boundary layer (Fig. 12a), indicated by the linear decrease of wind with decreasing height. Vertical scales of wind fluctuations in both speed and direction on the order of 200 m are well resolved by several fast-fall XDDs.

5. Data variance

As with the XDD fast and slow fall speed profiles described in Fig. 9a, the slow-fall GPS wind speeds and directions in Figs. 12a,b are much noisier than the fast-fall winds. Figure 13 illustrates a probability plot, similar to a cumulative frequency distribution, of differences between raw and smoothed slow- and fast-fall wind speed profile data. A 12-point running average was used to produce the smooth profile from which the raw data values were differenced. One can see from the difference in the slopes between slow- and fast-fall wind speed differences and the linearly fitted lines, representing normal probability distributions, that there is about a

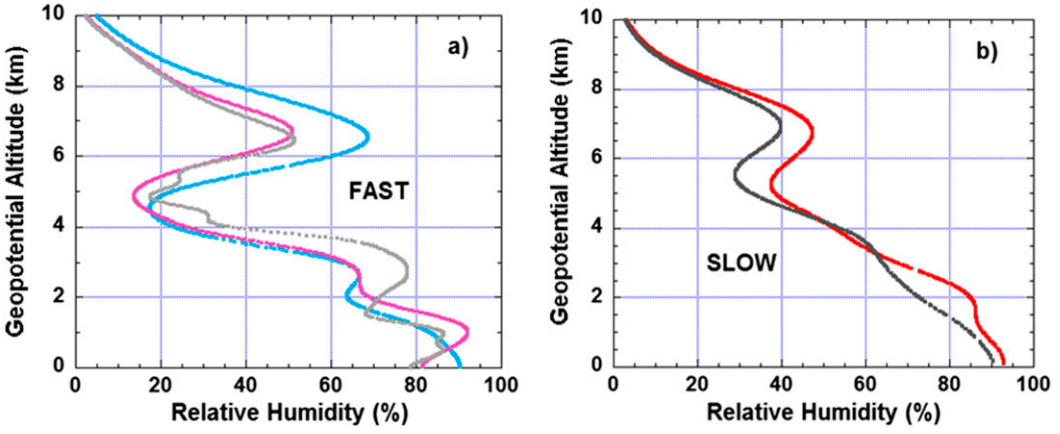

FIG. 10. Profiles of RH for (a) fast-fall profiles and (b) slow-fall profiles. The humidity sensor corresponding to the dark blue slow-fall profile position failed. Colors indicating profile locations are as in Fig. 8.

factor of 4 difference in the variance between the slow- and fast-fall XDD raw data. For example, the 95% probability value for the slow-fall wind speed differences are on order of 1.5 m s^{-1}, while the 95% probability value for the fast-fall sondes is approximately 0.4 m s^{-1}.

Histograms of high-frequency variances for observed XDD parameter raw data from the DC-8 flight are compared with those from RD-94 raw sonde data from the Twin Otter flights in Figs. 14a–e. DC-8 data from three fast-mode and three slow-mode XDDs are combined in each histogram. The histograms of variance shown are the absolute value of the variance for the difference between the reported data and smoothed data using a six-point high-pass binomial filter from 10 s after launch to an altitude 100 m above the boundary layer transition. For simplicity we identify this as the "flight variance," as it is a result of the combined effects of real atmospheric profile variance, instrument noise, and the effects of perturbations in sonde velocity on the measurements.

The slow-fall variances seen in the XDDs from the Twin Otter (not shown) are nearly identical to those from the slow-fall XDD data from the DC-8 tests (Figs. 14a–e), differing in both RMS variance and mean absolute variance by less than 20%, for all parameters except temperature. The DC-8 XDD slow- and fast-fall temperature variance was nearly twice that of the Twin Otter XDD profile variance.

The relative humidity (RH) variances for the slow-fall DC-8 XDDs and the Twin Otter RD-94s are considerable and appear to be a result of differences in the instrument time constants. The RD-94 RH sensor is faster, and we expect it to respond to atmospheric variances to a greater degree than the XDD. The population of the

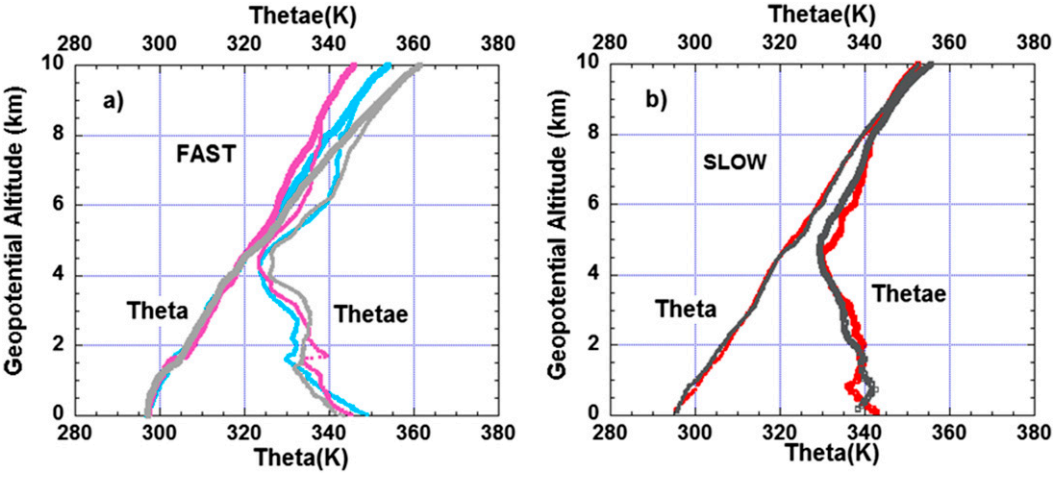

FIG. 11. Profiles of θ and θe for (a) fast-fall profiles and (b) slow-fall profiles. Colors indicating profile locations are as in Fig. 8.

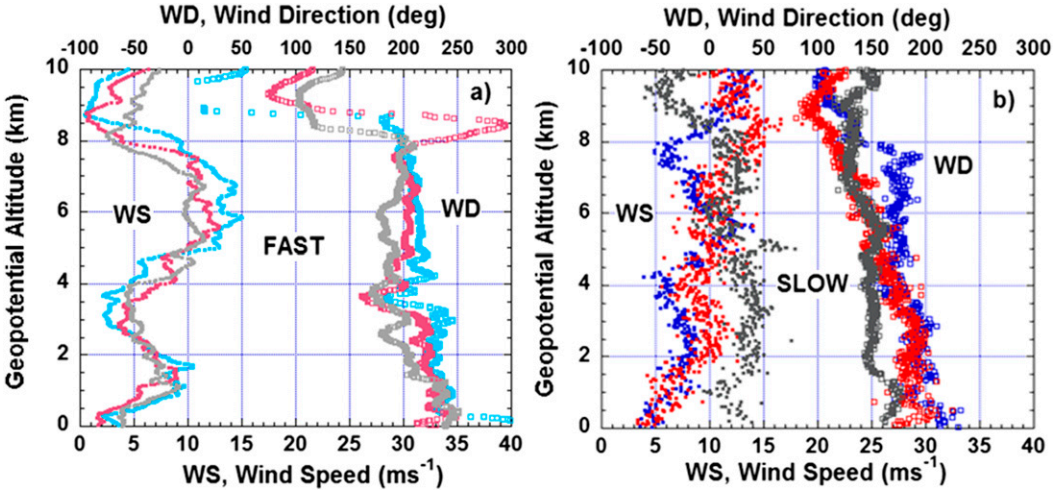

FIG. 12. WS and WD profiles for (a) fast-fall sondes and (b) slow-fall sondes. Colors for specific slow- and fast-fall sonde locations are as in Fig. 8. WS on left side of each panel and WD (divided by 10) on right side of each panel.

extreme RH outliers for the RD-94, summed for all histograms in the last bin, suggests that, despite the faster frequency response of the sensor, occasional outliers occur.

Figures 14a–e show that the number distribution of noise about the mean is greater for the slow-fall sondes than for the fast-fall for pressure, wind speed, and fall speed in Figs. 14a,e, respectively. Values are larger and the distribution is broader, indicating more outliers for the slow-fall sondes than for the fast-fall sondes. For temperature and humidity, the number distribution for noise is about the same for slow- and fast-fall sondes.

6. XDD deployment from WB-57

The HDSS unmanned Mark-B system was tested on NASA's WB-57, operating from Ellington Field during the period 13–19 November 2013. Three flights were conducted along a racetrack pattern from just offshore from CRP to BRO. Flights were approximately 2.5 h each, approximately 1100–1330 UTC, timed to overlap with early morning 1200 UTC NWS radiosonde ascents from CRP and BRO. The first two shakedown flights identified several integration problems on the new aircraft platform. These were corrected, resulting in a third successful flight on 19 November.

Planned (yellow) and actual (red) flight tracks for the third flight on 19 November are shown in Fig. 15, superimposed upon a BRO radar image and a GOES IR satellite image using NASA's Mission Tool Suite (MTS) flight monitoring system. The latency on the weather radar was about 5 min but closer to 1 h for the satellite. For this reason the radar and IR cloud features do not align perfectly. A total of 23 XDD dropsondes were successfully launched. A series of six successful sondes were deployed in less than 1 min, with all transmitting simultaneously, as the WB-57 flew over the minisquall line just east of the racetrack pattern, shown from the forward-looking HDSS camera in Fig. 16. To verify safe fuselage separation during ejection, the backseat observer monitored the HDSS aft- and forward-looking cameras. Camera imagery showed conclusively that each XDD fell away from the aircraft immediately, posing no threat to the aircraft. These cameras also

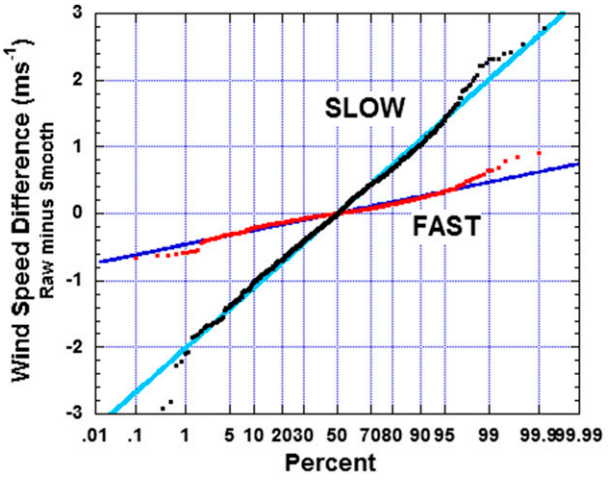

FIG. 13. Probability diagram showing percent differences for raw minus smooth (five-point running mean) WD difference for fast-fall (red dots) and slow-fall (black dots) sonde profiles. Dark and light blue lines indicate a linear best-fit normal probability distribution to the fast- and slow-fall differences, respectively. The 95% values for fast- and slow-fall sonde profiles are 0.35 and 1.50 m s^{-1}, respectively.

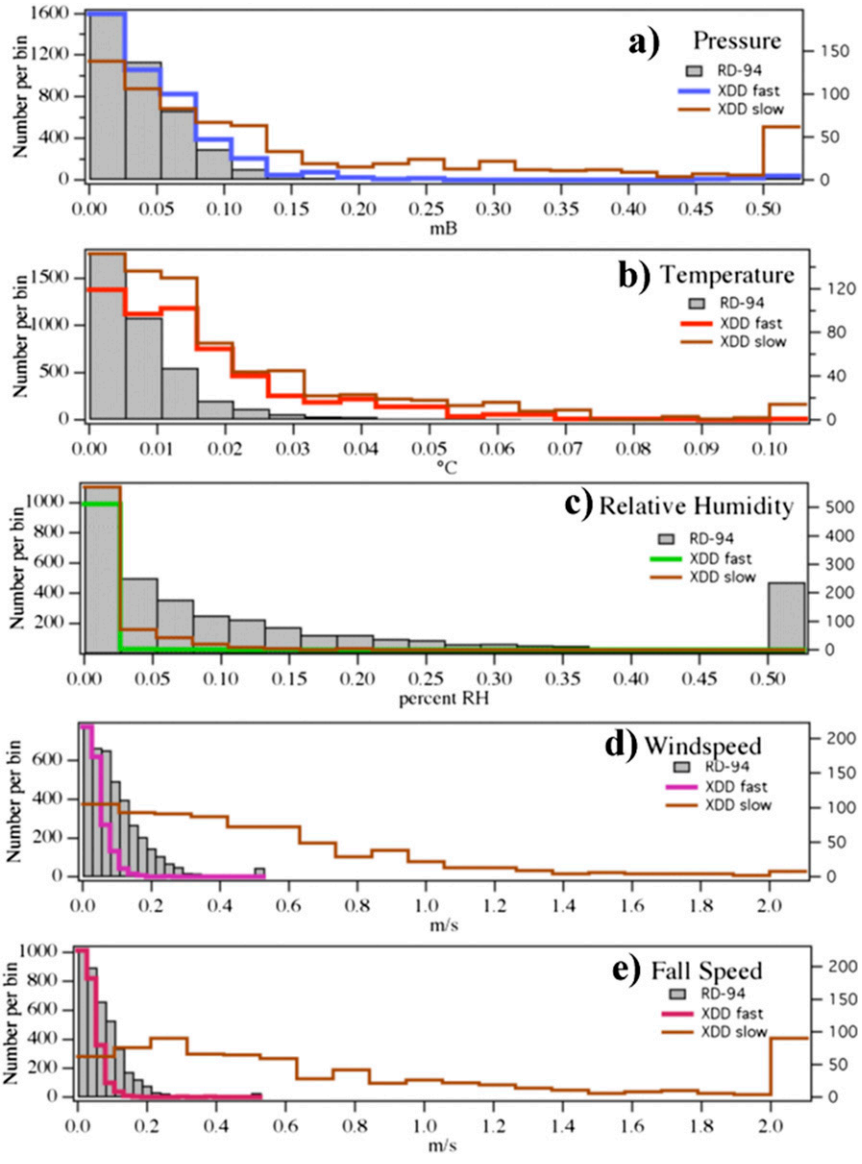

FIG. 14. Histograms of "flight variance" for (a) pressure, (b) temperature, (c) RH, (d) WS, and (e) sonde fall speed measured by XDD sondes deployed during the DC-8 flight and by RD-94 sondes deployed during Twin Otter flights.

proved extremely useful in enhancing situational awareness regarding flight progress relative to cloud features and rain areas for the science team on the ground via the Ku-band satcom link.

In addition to the first availability of the WB-57 on NASA's MTS, the ground science team was able to monitor aircraft track, weather system evolution, and HDSS function during the aircraft flight via a web-based interface module, now an integral part of HDSS. This display shows the status of XDD dropsondes not yet released in each of the two redundant ADDs, the telemetry status of deployed XDDs, the trajectory/PTU data plots, views from forward/aft cameras, the status of the Ku-band communication link, and an iChat window for text communication between the mission scientist and the onboard WB-57 mission manager.

Wind profiles derived from two XDDs and the corresponding NWS radiosonde ascents at CRP and BRO are shown in Fig. 17. The XDDs were deployed during the 1.5-h period it took for the radiosondes to ascend from the surface to 20-km (~70 mb) altitude. Similar wind perturbations appear in both the XDD and radiosonde profile pairs at both the north (near CRP) and south (near BRO) ends of the flight line. These profiles

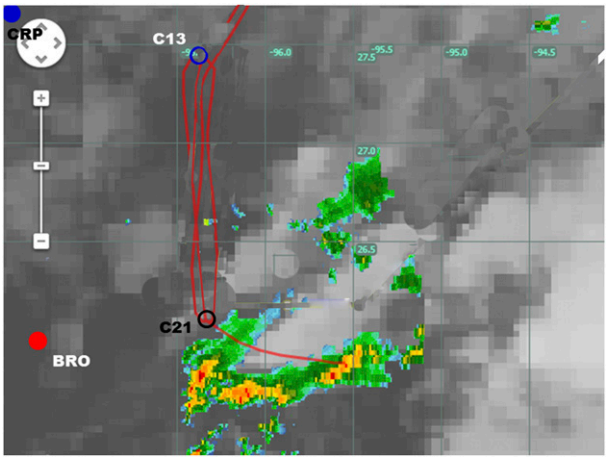

FIG. 15. WB-57 test flight track as flown on 19 Nov 2013. The location of the BRO and CRP radiosonde stations are shown in red and blue, respectively. The locations are also shown of the two sample XDDs: the slow-fall sonde, C13, deployed off shore from CRP, and C21, deployed off shore from BRO. BRO radar display is overlaid on GOES geostationary satellite IR image.

FIG. 16. Photo from the forward-looking, belly-mounted WB-57 camera documenting deployment of XDD (foreground left) at the beginning of a WB-57 sonde-deployment flight leg over the clouds associated with a squall line off the Texas coast (background right).

illustrate the vertical structure of a subtropical jet with maximum winds of 30 m s^{-1} and different mean velocity profiles below the maximum at CRP and BRO, but very similar perturbations, all of which were well resolved by the XDDs. This upper-level feature was just behind a cold front that had passed off the Texas coast the day before the flight. Of particular interest is the capability shown by this plot that the XDDs resolve all the fine-scale detail measured by the radiosondes, including fluctuations on the scale of 200–300 m. Both the XDD and CRP radiosonde observed a low-level wind maximum (from the northeast) at the north end of the WB-57 racetrack, consistent with its position farther behind the cold front and more well-established northeasterly flow. On this basis we judge this profile comparison to be reasonable. No intercomparison datasets in high-shear environments were available during the three sonde comparison periods, discussed here. However, subsequent XDD deployments into Hurricane Gonzalo in 2014 and Hurricanes Marty, Joaquin, and Patricia in 2015, results of which are given in Doyle et al. (2016, manuscript submitted to *Bull. Amer. Meteor. Soc.*), have shown reasonable wind shear values in excess of 12 m s^{-1} km^{-1} that were well resolved by multiple XDD sondes.

Figure 18 illustrates the comparison of the temperature and humidity profiles observed from XDD dropsonde "C21" and the BRO radiosonde. Humidity from the XDD becomes unreliable above about 9 km, where the air temperature decreases below −30°C. Otherwise, humidities below 8 km reflect the same basic features as revealed by the radiosonde profile data, that is, dry midlevel air above 6 km, with a moist low level below consisting of high variability centered near 80%. The humidities near the surface observed by the BRO radiosonde over land are almost 100%, about 15% higher than observed by the XDD over the ocean. This again appears real, as fog was reported at BRO at the time of the radiosonde launch; there was no fog over the ocean. The moisture maxima observed by the radiosonde at 1, 3, and 5–6 km are well resolved by the XDD.

The C21 upper-level air temperatures from 13 to 16 km are warmer than the radiosonde by about 10°C. This difference may be real, as the XDD was dropped

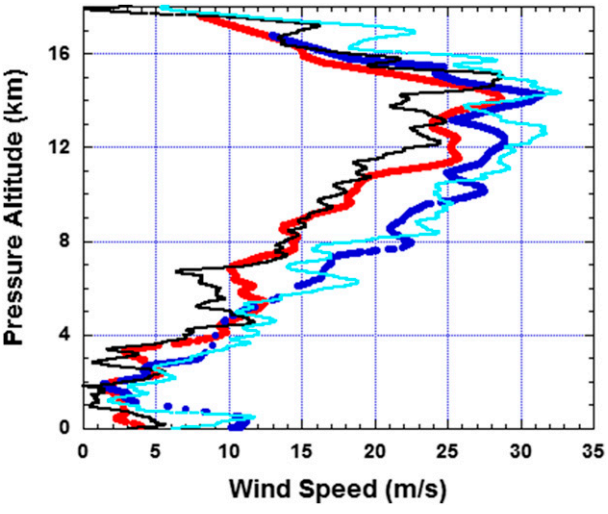

FIG. 17. Comparison of WS from C13 (dark blue), located due east of CRP, and C21 (red), located due east of BRO with radiosonde WS profiles from CRP (light blue) and BRO (black).

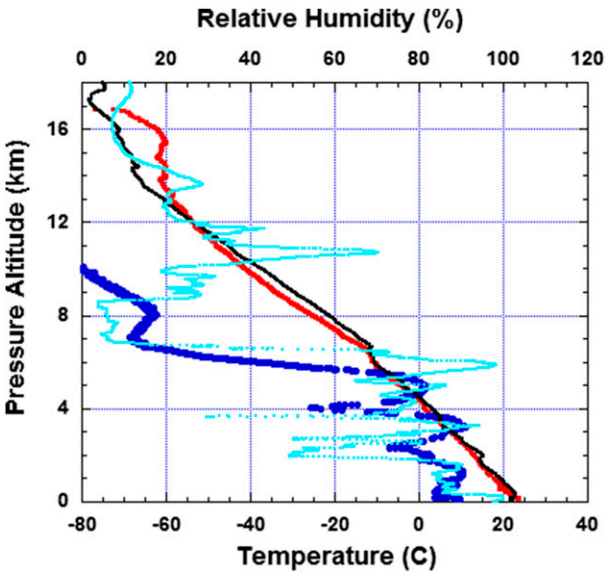

FIG. 18. Temperature and RH profile observed by sonde C21 (red and dark blue, respectively) located east of BRO with the BRO temperature and humidity (black and light blue, respectively).

through the trailing edge of the thunderstorm anvil from the cells just east of the WB-57 drop point. However, the warm XDD air temperature bias above 14 km may also be a result of slow adjustment to the environment after ejection from the aircraft at 18 km. Otherwise, the XDD air temperature exhibits a cold bias in midlevels of about −4°C, decreasing to −2°C in low levels below the frontal inversion at 6 km.

To demonstrate repeatability and to further support these observations, ''waterfall'' plots of temperature and wind speed were created from a second test flight on 20 November 2014, and are shown in Figs. 19a,b, in which 13 sondes were deployed in ''rapid fire'' fashion at 1-min intervals offshore from the Texas coast between CRP and BRO radiosonde ascents. These plots show that the intercomparison between the radiosonde ascents at BRO and CRP and the group of offshore XDD sondes is quite reasonable. In addition, while two sondes exhibit temperature offsets near the surface due to unknown instrument error, the remainder of the temperature and wind speed profiles exhibit reasonable repeatability in resolution of small-scale features in the soundings.

7. Humidity at very high altitudes

The WB-57 flights were the first XDD deployments above 10 km and by design they do not report RH below −40°C. Comparisons show that observed relative humidity is not reasonable at temperatures below −35°C. Upper-air measurements by balloonborne sondes also have been a very difficult issue that is well documented in the literature (Miloshevich et al. 2001; Vömel et al. 2007). It is made considerably more difficult from a dropsonde due to the relatively faster transit times and larger disequilibration between values at launch and initial environmental values.

Similar behavior was noted by Rivercombe et al. (2013), which showed large differences above 10-km altitude between the Global Hawk minisonde [deployed during the Hurricane and Severe Storm Sentinel (HS3) program] humidity values and the Scanning High-Resolution Interferometer Sounder (S-HIS) humidity values. S-HIS was initialized using European Centre for Medium-Range Weather Forecasts (ECMWF) model fields as a first guess in profile retrievals. S-HIS showed consistently higher humidities relative to the minisonde on the order of 40% above 400 mb for 14 intercomparisons during 2012. Cursory examination of 2013 minisonde and S-HIS humidity data indicates that this issue still persists (Rivercombe et al. 2013).

8. XDD infrared SST observations

The XDD is the first dropsonde platform to measure SSTir concurrent with PTH and wind profiles. The XDD accomplishes this via a broadband IR radiometer mounted on the sonde body, looking downward as the sonde falls. Figure 20 synthesizes all XDD SSTir observations deployed from the 1) Twin Otter over SSTs on order of 10°–12°C, 2) DC-8 over a range of SSTs from 17° to 22°C, and 3) WB-57 over SSTs on order of 26°–27°C. Observations 1 and 3 represented buoy bulk SST measurements. A second-order regression fit to the observations yields a fit to within 0.1°C and an R^2 value of 0.99. The curve indicates a bias with respect to in situ buoy and satellite SSTir values of 0.5°–1.0°C, over the midrange of the fit from 13° to 26°C.

9. Summary and conclusions

This paper describes the first field tests of the HDSS/XDD, developed to sample TC outflow structure with high spatial resolution and minimal data loss. This study shows that XDDs produce atmospheric temperature and wind profile measurements that resolve meteorological features consistent with 1) aircraft spiral descents, 2) conventional RD-94 dropsondes, and 3) operational radiosondes. Results suggest that XDDs have temperature and wind resolution similar to NWS radiosondes and RD-94 dropsondes while exhibiting lesser resolution and slower response for relative humidity. XDDs were biased warmer by about 1°C and drier by about 5%.

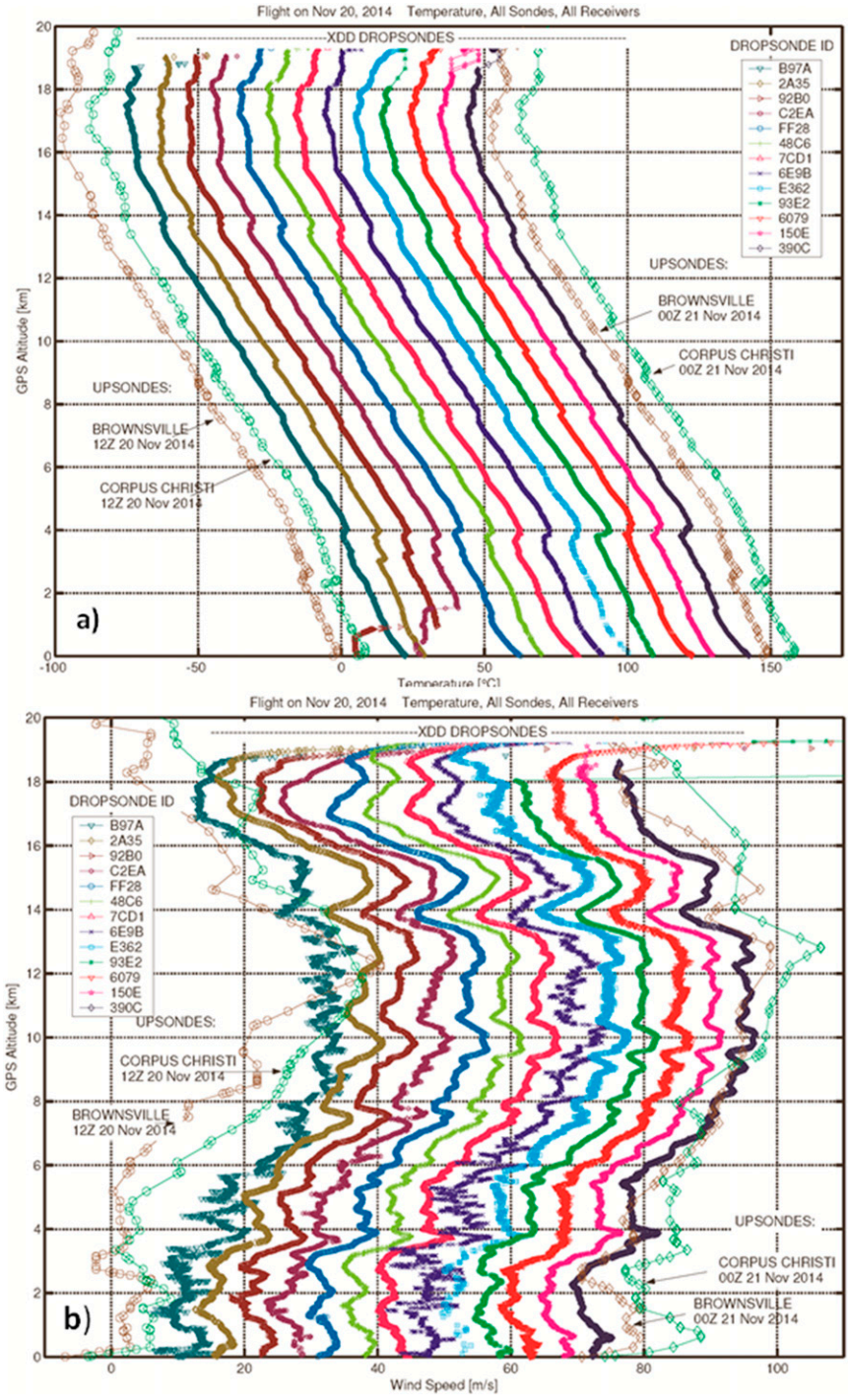

FIG. 19. Waterfall plot showing comparison of 13 XDD (a) temperature and (b) WS profiles from the test flight on 20 Nov 2014 with radiosonde ascents from BRO and CRP. Temperature profiles are offset by 10°C and WS profiles by 5 m s^{-1} from the initial scale.

These conclusions apply mainly to benign conditions and represent a first step to verify the applicability of a new dropsonde technology. Observations in the extreme high wind and heavy rainfall environment of major hurricanes have been obtained in 2015 with flights deploying over 750 XDDs into three major hurricanes in which supplemental NOAA and air force dropsonde deployments and flight-level measurements

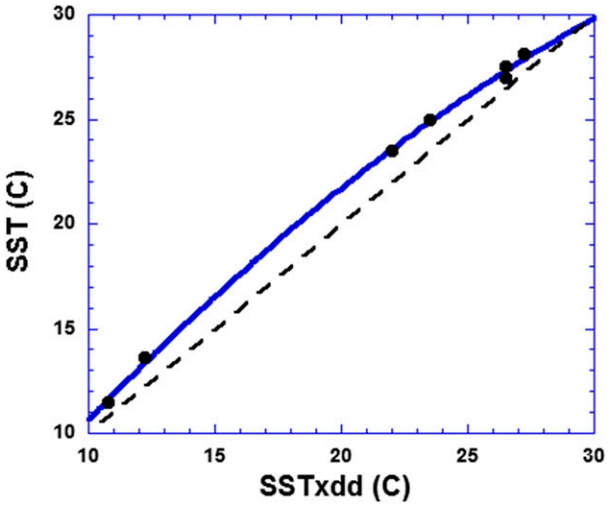

FIG. 20. XDD SST observations compared to buoy and satellite image SSTs from Twin Otter, DC-8, and WB-57 deployments off the California coast, off the Baja California coast east of ex-TC Cosme, and in the western Gulf of Mexico, east of the Texas coast, respectively. Dashed line indicates line of perfect agreement showing that the XDD exhibits a cool bias of 0.5°–1.0°C.

were also obtained and will be available for comparison in an effort to extend present results into extreme environments.

During the DC-8 XDD test flight conducted in the eastern tropical Pacific just east of decaying Tropical Storm Cosme and west of the Baja California Peninsula, a total of six sondes were deployed: three in spiral-dive slow mode and three in ballistic fast mode. The slow mode exhibited larger "flight variance" (as defined at the beginning of section 5) and greater numbers of data dropouts than did the fast mode, especially for the fall velocity and horizontal winds.

The WB-57 campaign demonstrated the HDSS from high altitude (18 km), operating autonomously, and dropping sondes into a precipitating squall line. The development effort for the XDDs has been driven by the goals of developing a capability to launch multiple sondes at high temporal rates (short spatial intervals on the order of tens of kilometers) and from high altitudes above the TC outflow layer (in excess of 20 km), so that sampling densities can be improved throughout the depth of the TC and other high-impact weather systems. While this study has demonstrated substantial progress toward these goals, further improvements in the HDSS/XDD were accomplished in 2015 with over 800 XDDs deployed from the WB-57 aircraft in two major hurricanes (Doyle et al. 2016, manuscript submitted to *Bull. Amer. Meteor. Soc.*). NASA has embarked on a program of refurbishment and modernization of the WB-57 aircraft, making it a valuable platform for high-altitude testing of various new technologies. In addition, NASA has undertaken the development of improved atmospheric-observing capability for use on the new generation of high-altitude, long-endurance (HALE) unmanned aerial vehicles (UAVs), such as the Global Hawk. The use of the Global Hawk UAV is providing the capability during HS3 of 24-h duration flights and the deployment of dropsondes to sample the entire depth of the storm, including outflow and inflow layer structures, on a continuous basis. Improvements to COAMPS-TC intensity and track forecasts using this new observational strategy in Hurricane Nadine from 2012 has been demonstrated for an initial case study (Doyle et al. 2014).

HDSS offers the potential to extend existing profiling strategies, combining new deployment schemes with these aircraft. While the impact of dropsonde observations has been shown to improve TC track forecast in the early days of omega and GPS dropsondes by 20% (Burpee et al. 1996), the *e*-folding time of this impact is estimated to be about 12 h (Aberson 2010). Use of NOAA Gulfstream IV (G-IV) flights for 12-hourly repeat observations has been shown to provide additional improvement over once-per-day sampling in TC track forecasting by allowing for daily time changes in initial conditions to be more accurately resolved (Aberson 2010). Use of the WB-57 in this same twice-a-day sampling strategy, but from 20-km altitude, may further enhance the impact of this strategy.

10. Future directions

An experiment was recently conducted during three flights in 3 days over Hurricane Gonzalo in 2014 in which over 100 XDD sondes were deployed from the NASA WB-57 flying at 20-km altitude with partial success due to sonde profiles being compromised by faulty wing antenna connections and a high background noise floor. Outflow jets with speeds up to 40 m s^{-1} were observed, exhibiting critical Richardson numbers in the high-shear zones above and below the core of the jets. Results describing similar features in 2015 flights are reported in Doyle et al. (2016, manuscript submitted to *Bull. Amer. Meteor. Soc.*).

These types of dropsonde deployments can enhance the capability of 3D Doppler sampling of winds only with PTH to provide input for the computation of a balanced initial state consistent with observations of both wind and mass fields. Use of the HDSS capability of rapid, multisonde deployments in concert with model predictions of high uncertainty/sensitivity regions of various key parameters opens a new era in TC surveillance

and reconnaissance. ''Burst'' sampling of SSTir by the XDDs can provide input to coupled TC models. NOAA launched a high-altitude Global Hawk dropsonde demonstration project called Sensing Hazards with Operational Unmanned Technology (SHOUT) in 2015 to test the real-time application of high-altitude sensing with burst sampling strategy using the NCAR NRD-94 ''minisonde'' system. In 2014 the Office of Naval Research initiated a TC research program called the Tropical Cyclone Intensity (TCI) program to investigate the relation of high-level outflow to TC intensity change using manned high-altitude WB-57 aircraft in cooperation with NASA using unmanned Global Hawk UAVs during the Hurricane and Severe Storm Sentinel (HS3) program, which ended in 2014. The NOAA SHOUT program in 2015 and SHOUT rapid response (SHOUTRR) in 2016, following on from HS3, launched over 839 minisondes in 16 flights. The TCI program was continued in 2015 with 840 XDDs deployed in three storms, including EPAC CAT 5 Hurricane Patricia and CAT4 Hurricane Joaquin (Doyle et al. 2016, manuscript submitted to *Bull. Amer. Meteor. Soc.*). These deployments ushered in a new era in tropical cyclone reconnaissance and surveillance with high-altitude dropsonde profiling as the focus.

Acknowledgments. The authors gratefully acknowledge the support of the Office of Naval Research for providing Twin Otter and WB-57 flight hour support and manpower support for P. Black and R. E. Lee under Contract N00014010-C-028. Mark Beaubien and Yankee Environmental Systems, Inc. were supported through SBIR Award N08-145. We express our thanks to Robert E. Lee, CMSgt (retired), for his assistance in the Twin Otter mission planning and execution. The authors wish to thank the technical staff at CIRPAS, especially Haflidi Jonsson, who maintained the Twin Otter data system. We thank the NASA Johnson Space Center, WB-57 Program Operations, for its extensive assistance with HDSS integration, especially the WB-57 program managers James Alexander and Tim Propp; the WB-57 flight crew, and the entire engineering and IT staff. We also wish to thank Patrick Finch and Aaron Duley, NASA Ames, for the display of WB-57 flight track on the NASA Mission Tools Suite, greatly improving situational awareness. Thanks are also extended to NWS personnel Steve Drillette, Jim Campbell, Lara Keys, and Ian Blaylock for providing radiosonde data. Finally, we thank the three anonymous reviewers of this paper for their intensive efforts in providing lengthy and insightful comments on this manuscript.

REFERENCES

Aberson, S. D., 2010: 10 years of hurricane synoptic surveillance (1997–2006). *Mon. Wea. Rev.*, **138**, 1536–1549, doi:10.1175/2009MWR3090.1.

——, 2011: The impact of dropwindsonde data from the THORPEX Pacific Area Regional Campaign and the NOAA hurricane field program on tropical cyclone forecasts in the Global Forecast System. *Mon. Wea. Rev.*, **139**, 2689–2703, doi:10.1175/2011MWR3634.1.

——, and J. L. Franklin, 1999: Impact on hurricane track and intensity forecasts of GPS dropwindsonde observations from the first-season flights of the NOAA Gulfstream-IV jet aircraft. *Bull. Amer. Meteor. Soc.*, **80**, 421–427, doi:10.1175/1520-0477(1999)080<0421:IOHTAI>2.0.CO;2.

Bender, M. A., I. Ginis, R. Tuleya, B. Thomas, and T. Marchok, 2007: The operational GFDL coupled hurricane–ocean prediction system and a summary of its performance. *Mon. Wea. Rev.*, **135**, 3965–3989, doi:10.1175/2007MWR2032.1.

Black, P. G., 2012: Tropical cyclone unusual intensity and structure change in the western North Pacific observed by reconnaissance aircraft during TPARC/TCS08 and ITOP/TCS10. *J. Trop. Cyclone Res. Rev.*, **1**, 75–88, doi:10.6057/2012TCRR01.09.

——, and Coauthors, 2007: Air–sea exchange in hurricane winds: Synthesis of observations from the Coupled Boundary Layer Air–Sea Transfer experiment. *Bull. Amer. Meteor. Soc.*, **88**, 357–374, doi:10.1175/BAMS-88-3-357.

Burpee, R. W., S. D. Aberson, J. L. Franklin, S. J. Lord, and R. E. Tuleya, 1996: The impact of omega dropwindsondes on operational hurricane track forecast models. *Bull. Amer. Meteor. Soc.*, **77**, 925–933, doi:10.1175/1520-0477(1996)077<0925:TIOODO>2.0.CO;2.

Chou, K.-H., C.-C. Wu, P.-H. Lin, S. D. Aberson, M. Weissmann, F. Harnisch, and T. Nakazawa, 2011: The impact of dropwindsonde observations on typhoon track forecasts in DOTSTAR and T-PARC. *Mon. Wea. Rev.*, **139**, 1728–1743, doi:10.1175/2010MWR3582.1.

D'Asaro, E., and Coauthors, 2011: Typhoon-ocean interaction in the western North Pacific: Part 1. *Oceanography*, **24** (4), 24–31, doi:10.5670/oceanog.2011.91.

——, and Coauthors, 2014: Impact of Typhoons on the Ocean in the Pacific. *Bull. Amer. Meteor. Soc.*, **95**, 1405–1418, doi:10.1175/BAMS-D-12-00104.1.

DeMaria, M., 2009: A simplified dynamical system for tropical cyclone intensity prediction. *Mon. Wea. Rev.*, **137**, 68–82, doi:10.1175/2008MWR2513.1.

——, 2010: Tropical cyclone intensity change predictability estimates using a statistical-dynamical model. *29th Conf. on Hurricanes and Tropical Meteorology*, Tucson, AZ, Amer. Meteor. Soc., 9C.5. [Available online at https://ams.confex.com/ams/29Hurricanes/techprogram/paper_167916.htm.]

——, and J. Kaplan, 1999: An updated Statistical Hurricane Intensity Prediction Scheme (SHIPS) for the Atlantic and eastern North Pacific basins. *Wea. Forecasting*, **14**, 326–337, doi:10.1175/1520-0434(1999)014<0326:AUSHIP>2.0.CO;2.

——, M. Mainelli, L. K. Shay, J. A. Knaff, and J. Kaplan, 2005: Further improvements in the Statistical Hurricane Intensity Prediction Scheme (SHIPS). *Wea. Forecasting*, **20**, 531–543, doi:10.1175/WAF862.1.

——, C. R. Sampson, J. A. Knaff, and K. D. Musgrave, 2014: Is tropical cyclone intensity guidance improving? *Bull. Amer. Meteor. Soc.*, **95**, 387–398, doi:10.1175/BAMS-D-12-00240.1.

Doyle, J. D., J. Moskaitus, P. Black, E. Hendricks, and P. A. Reinecke, 2014: Upper-level outflow, predictability and HS3 observation impact. *31st Conf. on Hurricanes and Tropical Meteorology*, San Diego, CA, Amer. Meteor. Soc., 8A.3. [Available online at https://ams.confex.com/ams/31Hurr/webprogram/Paper244211.html.]

Franklin, J. L., M. L. Black, and K. Valde, 2003: GPS dropwindsonde wind profiles in hurricanes and their operational implications. *Wea. Forecasting*, **18**, 32–44, doi:10.1175/1520-0434(2003)018<0032:GDWPIH>2.0.CO;2.

Gall, J. S., I. Ginis, S.-J. Lin, T. P. Marchok, and J.-H. Chen, 2011: Experimental tropical cyclone prediction using the GFDL 25-km-resolution global atmospheric model. *Wea. Forecasting*, **26**, 1008–1019, doi:10.1175/WAF-D-10-05015.1.

Gasiewski, A., A. Chaturvedi, E. McIntyre, D. M. Kraft, P. O. G. Persson, M. Tjernstrom, M. Beaubien, and W. Jeffries, 2009: Use of a new generation of dropsondes during the 2008 Arctic Mechanisms for the Interaction of the Surface and Atmosphere (AMISA) campaign. *10th Conf. on Polar Meteorology and Oceanography*, Madison, WI, Amer. Meteor. Soc., 10.5. [Available online at https://ams.confex.com/ams/10POLAR/webprogram/Paper152908.html.]

Gupta, K., P. K. Ghosh, R. N. Piplia, and A. Dey, 2010: A comparative study of Viterbi and Fano decoding algorithm for convolution codes. *AIP Conf. Proc.*, **1324**, 34, doi:10.1063/1.3526231.

Hock, T. F., and J. L. Franklin, 1999: The NCAR GPS dropwindsonde. *Bull. Amer. Meteor. Soc.*, **80**, 407–420, doi:10.1175/1520-0477(1999)080<0407:TNGD>2.0.CO;2.

Jin, H., M. S. Peng, Y. Jin, and J. D. Doyle, 2014: An evaluation of the impact of horizontal resolution on tropical cyclone predictions using COAMPS-TC. *Wea. Forecasting*, **29**, 252–270, doi:10.1175/WAF-D-13-00054.1.

Jones, T. A., D. J. Cecil, and M. DeMaria, 2006: Passive-microwave-enhanced Statistical Hurricane Intensity Prediction Scheme. *Wea. Forecasting*, **21**, 613–635, doi:10.1175/WAF941.1.

Kaplan, J., M. DeMaria, and J. A. Knaff, 2010: A revised tropical cyclone rapid intensification index for the Atlantic and eastern North Pacific basins. *Wea. Forecasting*, **25**, 220–241, doi:10.1175/2009WAF2222280.1.

Kim, H.-S., C. Lozano, V. Tallapragada, D. Iredell, D. Shenin, H. L. Tolman, V. M. Gerald, and J. Sims, 2014: Performance of ocean simulations in the coupled HWRF–HYCOM Model. *J. Atmos. Oceanic Technol.*, **31**, 545–559, doi:10.1175/JTECH-D-13-00013.1.

Klotz, B. W., and E. W. Uhlhorn, 2014: Improved stepped frequency microwave radiometer tropical cyclone surface winds in heavy precipitation. *J. Atmos. Oceanic Technol.*, **31**, 2392–2408, doi:10.1175/JTECH-D-14-00028.1.

Knaff, J. A., C. R. Sampson, and M. DeMaria, 2005: An operational Statistical Typhoon Intensity Prediction Scheme for the western North Pacific. *Wea. Forecasting*, **20**, 688–699, doi:10.1175/WAF863.1.

Miloshevich, L. M., H. Vömel, A. Paukkunen, A. J. Heymsfield, and S. J. Oltmans, 2001: Characterization and correction of relative humidity measurements from Vaisala RS80-A radiosondes at cold temperatures. *J. Atmos. Oceanic Technol.*, **18**, 135–156, doi:10.1175/1520-0426(2001)018<0135:CACORH>2.0.CO;2.

Persson, P. O. G., 2010: Summary of meteorological conditions during the Arctic Mechanisms for the Interaction of the Surface and Atmosphere (AMISA) intensive observation periods. NOAA Tech. Memo PSD-314, 57 pp.

Rivercombe, H., and Coauthors, 2013: Scanning HIS: Advance IR Sounder for HS3. HS3 Science Team and Deployment Preparation Meeting, Moffett Field, CA, NASA. [Available online at https://espo.nasa.gov/missions/hs3/content/HS3_Science_Presentations.]

Tallapragada, V., C. Kieu, Y. Kwon, S. Trahan, Q.-F. Liu, Z. Zhang, and I.-H. Kwon, 2014: Evaluation of storm structure from the operational HWRF model during 2012 Implementation. *Mon. Wea. Rev.*, **142**, 4308–4325, doi:10.1175/MWR-D-13-00010.1.

Uhlhorn, E. W., and P. G. Black, 2003: Verification of remotely sensed sea surface winds in hurricanes. *J. Atmos. Oceanic Technol.*, **20**, 99–116, doi:10.1175/1520-0426(2003)020<0099:VORSSS>2.0.CO;2.

——, ——, J. L. Franklin, M. Goodberlet, J. Carswell, and A. S. Goldstein, 2007: Hurricane surface wind measurements from an operational stepped frequency microwave radiometer. *Mon. Wea. Rev.*, **135**, 3070–3085, doi:10.1175/MWR3454.1.

Verver, G., M. Fujiwara, P. Dolmans, C. Becker, P. L. Fortuin, and L. Miloshevich, 2006: Performance of the Vaisala RS80A/H and RS90 Humicap sensors and the Meteolabor "Snow White" chilled-mirror hygrometer in Paramaribo, Suriname. *J. Atmos. Oceanic Technol.*, **23**, 1506–1517, doi:10.1175/JTECH1941.1.

Vömel, H., and Coauthors, 2007: Radiation dry bias of the Vaisala RS92 humidity sensor. *J. Atmos. Oceanic Technol.*, **24**, 953–963, doi:10.1175/JTECH2019.1.

Wang, J.-H., and Coauthors, 2015: A long-term, high-quality, high-vertical-resolution GPS drosponde dataset for hurricane and other studies. *Bull. Amer. Meteor. Soc.*, **96**, 961–973, doi:10.1175/BAMS-D-13-00203.1.

Weissmann, M., and Coauthors, 2011: The influence of assimilating dropsonde data on typhoon track and midlatitude forecasts. *Mon. Wea. Rev.*, **139**, 908–920, doi:10.1175/2010MWR3377.1.

Wu, C.-C., K.-H. Chou, P.-H. Lin, S. D. Aberson, M. S. Peng, and T. Nakazawa, 2007: The impact of dropwindsonde data on typhoon track forecasts in DOTSTAR. *Wea. Forecasting*, **22**, 1157–1176, doi:10.1175/2007WAF2006062.1.